Title

Three-dimensional imaging from single-element holographic data.

Journal

Journal of the Optical Society of America A, 38(2)

ISSN

1084-7529

Authors

Moscoso, M
Novikov, A
Papanicolaou, G
et al.

Publication Date

2021-02-01

DOI

10.1364/josaa.402396

Three dimensional imaging from single element holographic data

Miguel Moscoso*, Alexei Novikov†, George Papanicolaou‡, Chrysoula Tsogka§

Abstract

We present a holographic imaging approach for the case in which a single source-detector pair is used to scan a sample. The source-detector pair collects intensity-only data at different frequencies and positions. By using an appropriate illumination strategy we recover field cross-correlations over different frequencies for each scan location. The problem is that these field cross-correlations are asynchronized, so they have to be aligned first in order to image coherently. This is the main result of the paper: a simple algorithm to synchronize field cross-correlations at different locations. Thus, one can recover full field data up to a global phase that is common to all scan locations. The recovered data are, then, coherent over space and frequency so they can be used to form high-resolution three dimensional images. Imaging with intensity-only data is therefore as good as coherent imaging with full data. In addition, we use an ℓ_1-norm minimization algorithm that promotes the low dimensional structure of the images allowing for deep high-resolution imaging.

1 Introduction

Imaging with intensity-only measurements is an important and challenging problem in fields such as x-ray crystallography, laser optics, or electron microscopy. Only the magnitude squared of the spatial Fourier transform of the image can be measured while the phase is lost. This raises the well-known phase retrieval problem, which attempts to reconstruct the missing phases. Loss of phase information occurs in optics as well because optical sensors such as CCD cameras cannot record phases. Phase retrieval is also important in applications where the sampled phase information is polluted by unavoidable phase errors.

Two well known approaches to the phase retrieval problem in optics are holography [1] and coherent diffraction imaging [2]. In holography, the reconstruction of the missing phases is done with a controlled reference beam that creates interference fringes within the diffraction pattern that are proportional to the modulus of the Fourier transform of the object to be imaged. The fringes are related in a known way to the unrecorded phases. Coherent diffraction imaging, however, does not use a reference beam to recover the missing phase information. The images are formed using only intensity patterns. Yet, since wave propagation is coherent, the phases are encoded in these patterns and can be, in principle, recovered using iterative phase-retrieval algorithms [3] that exploit redundancies in the data, such as oversampling of the diffraction patterns. This is also the approach in ptychography that records the patterns from a series of partially overlapping regions, giving rise to data redundancies [4]. Because these imaging modalities generate two-dimensional diffraction patterns, depth-resolved images are formed by assembling these patterns using tomographic methods. This, for example, allows for non-invasive, free-label cell imaging in biomedical research that requires minimal cell manipulation [6, 5].

On the other hand, optically sectioning of a sample often requires its mechanical movement rotating it around a fixed axis to acquire a full set of projections. Such acquisition procedure may introduce

[1]Department of Mathematics, Universidad Carlos III de Madrid, Leganes, Madrid 28911, Spain
[2]Mathematics Department, Penn State University, University Park, PA 16802
[3]Department of Mathematics, Stanford University, Stanford, CA 94305
[4]Department of Applied Mathematics, University of California, Merced, 5200 North Lake Road, Merced, CA 95343

unwanted artifacts in the reconstructions due to translational and rotational misalignments that degrade the quality of the resulting images [7]. To reduce this problem, we propose to produce holographic data from intensity measurements. Since these data are inherently centered, this approach has the advantage of being fully alignment-free allowing for reconstructions even in the presence of constant drifts or random vibrations due to mechanical rotations of the sample during the registration process. The method, though, requires a careful control of the source signals including the ability to create narrowband illuminations.

It is a direct method and, therefore, iterative phase-retrieval algorithms are avoided, so there are no convergence issues. It does not require oversampling neither, as it is often the case in coherent diffraction imaging or ptychography.

In addition, we also propose to use an ℓ_1-norm minimization method that allows for high-resolution imaging. The basic idea is that, often, the images have a low dimensional structure, so they admit a sparse representation in certain bases, and this knowledge makes possible to recover the fine scale information lost in the data when we promote it with these methods [8, 9, 10].

We consider here a moving source-detector pair that scans a sample. For example, the source-detector pair may rotate around a circle acquiring the reflected data from the sample at different angles and frequencies. Alternatively, the sample is rotated around its center of symmetry while the source-detector pair remains fixed. The sample is far from the source-detector pair so the illumination is a plane wave. Under these conditions, we solve a phase retrieval problem for one dimensional Fourier data for each source-detector position. Different acquisition schemes maybe considered. The position of the detector with respect to the source maybe fixed throughout the dataset acquisition process or the source location could be fixed and only the detector maybe moving. Source and detector can be placed on the same side of the sample (reflection mode), or on the other side (transmission mode). Thus, light signals from the sample can be recorded from both the upper surface or transmitted through it, as it is typical in tomographic reconstructions.

To fix ideas, let us consider M point-like reflectors with reflectivities $\rho_j,\ j=1,\dots,M$. They are within a size a small box referred to as the imaging window (IW), which is discretized using K grid points $\boldsymbol{y}_k$, $k=1,\dots,K$. Let us denote by $\boldsymbol{x}_r$ the photodetector location and by $\boldsymbol{x}_s$ the source location. Then, when we illuminate the IW with a multifrequency vector $\boldsymbol{e}=(e_1,e_2,\dots,e_S)$, the collected intensity by the photodetector is given by

$$|b_p(\boldsymbol{e})|^2 = C\left|\sum_{l=1}^{S}\sum_{k=1}^{K}\rho_k e_l e^{i\,\frac{\omega_l}{c}d_p(y_k)}\right|^2, \tag{1}$$

where C is a geometric factor, $i=\sqrt{-1}$ and $d_p(\boldsymbol{y}_k)=|\boldsymbol{x}_r-\boldsymbol{y}_k|+|\boldsymbol{x}_s-\boldsymbol{y}_k|$ denotes the total distance from the source to the point $\boldsymbol{y}_k$ and from to the point $\boldsymbol{y}_k$ to the receiver. We use the notation $p=p(\boldsymbol{x}_s,\boldsymbol{x}_r)$ to indicate the dependance of the measurements (and the distance) on the position of the source-detector pair. In (1), we ascribe the reflectivity ρ_j to the grid point that contains an object with that reflectivity. Otherwise, a grid point has reflectivity zero. A basic example of an illumination vector is $\boldsymbol{e}_l$, the vector with 1 in the l-th coordinate and 0's elsewhere. It represents an illumination with amplitude 1 and phase 0 at frequency ω_l.

Moreover, we assume that the reflectivity vector $\boldsymbol{\rho}=[\rho_1,\rho_2,\dots,\rho_K]$ is M-sparse with $M\ll K$. This is often true in applications where the reflectivity to be imaged does not occupy the entire scene but rather a small part of the IW. For example, gold nanoparticles 50200 nm in diameter are particularly convenient for imaging in vivo since their high scattering cross section makes them very bright compared to the surrounding medium [11, 12, 13]. These particles scatter light nearly equally in all directions, so we assume isotropic scattering.

We stress that in this work we assume that the solution is sparse in its canonical basis for clarity of exposition only. If $\boldsymbol{\rho}$ is not sparse in the physical space, we can apply a sparsifying transform Λ, such as $\boldsymbol{\rho} = \Lambda \boldsymbol{x}$, where $\boldsymbol{x}$ is a sparse vector, and solve for $\boldsymbol{x}$ instead [14, 15]. In this new basis, simplicity or structure shows up as sparsity in $\boldsymbol{x}$.

The most difficult task is to determine the support of this vector, i.e., the values of $\boldsymbol{y}_k$ such that $\rho_k \neq 0$. This is the combinatorial part of the imaging problem which is NP-hard [16]. Once the support is known, it is straightforward to estimate the values of the reflectivities by restricting the inversion to the support. Note that if the detectors can record the phases it would be trivial to determine the distances $|\boldsymbol{x}_r - \boldsymbol{y}_k| + |\boldsymbol{x}_s - \boldsymbol{y}_k|$ by a simple inverse Fourier transform of $\boldsymbol{b}_p = [b_p(\boldsymbol{e}_1), b_p(\boldsymbol{e}_2), \ldots, b_p(\boldsymbol{e}_S)]^t$ for each source-detector position pair $(\boldsymbol{x}_s, \boldsymbol{x}_r)$. Then, the locations $\boldsymbol{y}_k$ of the objects would be obtained by well-established imaging methods.

When phases are missing from the measurements, as in (1), we cannot determine the distances $|\boldsymbol{x}_r - \boldsymbol{y}_k| + |\boldsymbol{x}_s - \boldsymbol{y}_k|$ directly by an inverse Fourier transform. We can determine, however, pairwise distances between the targets locations. Still, the problem is that the pairwise distances for each source-detector position are not referred to the same point and, thus, we have to refer them to a common one if we want to image coherently.

The method has two stages. First, from the intensity data at each source-detector position, we recover field cross-correlations corresponding to coherent sources of different frequencies. These cross-correlations are the same as the ones obtained from full data, up to a global phase that is different for each source-detector position. Hence, the field cross-correlations obtained from intensity data cannot be used coherently to determine the locations $\boldsymbol{y}_k$ of the targets. To use them coherently over all scan positions they need to be synchronized or aligned first. To do so, we refer the unknown global phases to the total reflectivity, which is a common quantity to all scan positions. This is the second stage of the imaging method introduced in [17]. With this strategy, we show that imaging with intensity-only data is as good as imaging with full data.

We stress that, for this method to work, one has to have good control of the light sources. Any acquisition geometry is allowed either in reflection or in transmission mode. We have observed, however, that source-detector configurations which enable greater phase diversity in the data are more robust and provide more accurate reconstructions. In particular our simulations suggest that when the source and the detector are moving on a circle and are diametrically opposed one to another, forming angles close to 180°, the inversion is more unstable and sensitive to noise in the data.

2 Cross correlation-based strategy

We can recover field cross-correlated data [19, 18, 20]

$$m_{ll'}^p = \overline{b_p(\boldsymbol{e}_l)} b_p(\boldsymbol{e}_{l'}), \quad l, l' = 1, \ldots, S, \tag{2}$$

from intensity measurements using the polarization identities

$$\mathrm{Re}(m_{ll'}^p) = \frac{1}{2} \left(|b_p(\boldsymbol{e}_l + \boldsymbol{e}_{l'})|^2 - |b_p(\boldsymbol{e}_l)|^2 - |b_p(\boldsymbol{e}_{l'})|^2 \right), \tag{3}$$

$$\mathrm{Im}(m_{ll'}^p) = \frac{1}{2} \left(|b_p(\boldsymbol{e}_l - i\, \boldsymbol{e}_{l'})|^2 - |b_p(\boldsymbol{e}_l)|^2 - |b_p(\boldsymbol{e}_{l'})|^2 \right), \tag{4}$$

where $\mathrm{Re}(\cdot)$ and $\mathrm{Im}(\cdot)$ denote the real and imaginary parts of a complex number, respectively. Naturally, $|b_p(\boldsymbol{e}_l + \boldsymbol{e}_{l'})|^2$ represents the intensity measured when the detector is positioned at $\boldsymbol{x}_r$ and two signals of frequencies ω_l and $\omega_{l'}$ are sent simultaneously from $\boldsymbol{x}_s$, and $|b_p(\boldsymbol{e}_l - i\, \boldsymbol{e}_{l'})|^2$ represents the intensity measured when the signal of frequency $\omega_{l'}$ has a phase shift of $\pi/2$ rad with respect to the signal of frequency ω_l. This can be easily accomplished by using a quarter-wave plate.

Equations (3)-(4) show that we can recover the field cross-correlations (2) using an appropriate protocol of illuminations, even when phases are not recorded. These cross-correlations $m^p_{ll'}$ are obtained through quadratic quantities and, hence, there is a global phase that cannot be determined for each position of the source-detector pair. To sum up, when only intensities are measured we can recover field cross-correlations up to a global phase that is independent of frequency but that depends on the the source-detector pair position. These global phases are essential if we want to superpose images coherently for all measurements locations. Indeed, the unknown phase for each location means that we can only determine pairwise differences of the targets locations. This is the main difficulty that needs to be overcome when the data acquisition system, or the sample, is moved to acquire information for imaging.

Recovery of the cross-correlations (2) up to a global phase amounts to recovering the full data up to a global phase as well. Indeed, setting the phase of $b_p(\boldsymbol{e}_1)$ equal to zero, we can form the vector $\boldsymbol{\beta}_p$ with components $\beta_{p1} = \sqrt{m^p_{11}}$ and $\beta_{pl} = m^p_{1l}/\sqrt{m^p_{11}}$, $l = 2, \dots, S$, that only differs from the full data vector $\boldsymbol{b}_p$ in a global phase factor $e^{i\theta_p}$, i.e., $\boldsymbol{\beta}_p = \boldsymbol{b}_p\, e^{i\theta_p}$.

Thus, by using (1) we can find the locations of the targets associated to each source photodetector position, up to a reference point, by solving the system

$$\mathcal{A}_p \boldsymbol{\rho}_{d_p} = \boldsymbol{\beta}_p \tag{5}$$

for the reflectivity vector $\boldsymbol{\rho}_{d_p}$, where

$$\mathcal{A}_p = \begin{bmatrix} e^{i\,\frac{\omega_1}{c} d_p(y_1)} & e^{i\,\frac{\omega_1}{c} d_p(y_2)} & \dots & e^{i\,\frac{\omega_1}{c} d_p(y_k)} \\ e^{i\,\frac{\omega_2}{c} d_p(y_1)} & e^{i\,\frac{\omega_1}{c} d_p(y_2)} & \dots & e^{i\,\frac{\omega_2}{c} d_p(y_K)} \\ \vdots & \vdots & & \vdots \\ e^{i\,\frac{\omega_S}{c} d_p(y_1)} & e^{i\,\frac{\omega_S}{c} d_p(y_2)} & \dots & e^{i\,\frac{\omega_S}{c} d_p(y_K)} \end{bmatrix}. \tag{6}$$

The subscript r is used to emphasize that (5) uses data recovered from one source photodetector position only. The vector $\boldsymbol{\rho}_{d_p}$ does not represent the true reflectivity vector, but the sum of the reflectivities located at the same distance $d_p(\boldsymbol{y}_k) = |\boldsymbol{x}_r - \boldsymbol{y}_k| + |\boldsymbol{x}_s - \boldsymbol{y}_k|$ from the source-detector. In model (5)-(6) we have assumed that the medium between the source-detector pair is homogeneous. If the measurements are taken from outside the sample and the boundaries are index mismatched, we would have to model it in (6).

For a sparse reflectivity vector, the solution $\boldsymbol{\rho}_{d_p}$ can be found by using ℓ_1-optimization algorithms. In the simulations shown below, we use a generalized Lagrangian multiplier algorithm (GeLMA) [21]. For noise-free data, exact recovery is guaranteed under the assumption that the mutual coherence of each matrix $\mathcal{A}_p$ is smaller than $1/(2M_p)$, M_p being the number of non zero components of $\boldsymbol{\rho}_{d_p}$. We recall that the mutual coherence of a matrix $\mathcal{A}$ is defined as

$$\mu = \max_{i \neq j} |\langle \boldsymbol{a}_i, \boldsymbol{a}_j \rangle| \,, \tag{7}$$

where $\boldsymbol{a}_i \in \mathbb{C}^N$ are the columns of $\mathcal{A}$ normalized to one. A measurement matrix is incoherent if μ is small. The value of μ depends on the properties of the imaging set-up, such as the (synthetic) aperture of the optical array or the sought image resolution. As a rule of thumb, the larger the optical aperture, the smaller μ, and the higher the resolution, i.e., the more image details we want to resolve, the larger μ is.

Once the solution vector $\boldsymbol{\rho}_{d_p} = [\rho_{p1}, \rho_{p2}, \dots, \rho_{pK}]$ has been found for each source-detector position (parametrized here by $p = 1, \dots, N$), we compute the total reflectivities $\sum_{k=1}^{K} \rho_{rk}$ seen by each source-photodetector, which is a common quantity for all of them that only differs in the unknown phase factors

$e^{i\theta_p}$. This motivates the key observation that we can refer all recovered quantities to the same global phase. To this end, we define

$$c_p = \frac{\sum_{k=1}^{K} \rho_{pk}}{\sum_{k=1}^{K} \rho_{1k}} = e^{i\,(\theta_p - \theta_1)},\ \ p = 1, \ldots, N. \tag{8}$$

The choice of $p = 1$ in the denominator is, of course, arbitrary. With this choice, $c_1 = 1$. Multiplying the recovered data vector $\boldsymbol{\beta}_p$ by the complex conjugate of (8), we get $\overline{c_p}\beta_{pl} = b_p(\boldsymbol{e}_l)e^{i\,\theta_1}$, $\forall\, p = 2, \ldots, N$, and $l = 1, \ldots, S$. This second step defines the holographically recovered data

$$\begin{aligned} b_1^h(\boldsymbol{e}_l) &= \beta_{1l},\ \forall\ l = 1, \ldots, S. \\ b_p^h(\boldsymbol{e}_l) &= \overline{c_p}\beta_{pl},\ \forall\, p = 2, \ldots, N \text{ and } l = 1, \ldots, S, \end{aligned} \tag{9}$$

whose phases are now coherent over different scan positions and frequencies. Thus, the images can be formed as if data with phases were recorded.

Indeed, once the data (9) are obtained, we can use any imaging method to determine the positions of the scatterers. Here we show results obtained with the traditional Kirchhoff migration (KM) imaging method and the ℓ_1-optimization approach. KM is a direct imaging ℓ_2-method [22] which can be written as

$$\rho^{KM}(\boldsymbol{y}_k) = \sum_{p=1}^{N} \sum_{l=1}^{S} e^{-i\,\frac{\omega_l}{c} d_p(y_k)}\, b_p^h(\boldsymbol{e}_l). \tag{10}$$

However, when the scene is sparse, meaning that only a few M components of $\boldsymbol{\rho}$ are different than zero so $M \ll K$, ℓ_1-optimization algorithms that solve [14, 16]

$$\min \|\boldsymbol{\rho}\|_{\ell_1}, \quad \text{subject to} \quad \mathcal{A}\,\boldsymbol{\rho} = \boldsymbol{b}^h, \tag{11}$$

can recover the true scene efficiently, even when the data are scarse so $N \ll K$. These methods provide better resolution than ℓ_2-methods but they are more sensitive to noise in the data, in general. In (11), we form $\mathcal{A}$ and $\boldsymbol{b}^h$ by stacking $\mathcal{A}_p$ and $\boldsymbol{b}_p^h = \overline{c_p}[\beta_{p1}, \beta_{p1}, \ldots, \beta_{pS}]$, respectively, so

$$\mathcal{A} = \begin{bmatrix} \mathcal{A}_1 \\ \mathcal{A}_2 \\ \vdots \\ \mathcal{A}_N \end{bmatrix}, \text{ and } \boldsymbol{b}^h = \begin{bmatrix} \boldsymbol{b}_1^h \\ \boldsymbol{b}_2^h \\ \vdots \\ \boldsymbol{b}_N^h \end{bmatrix}. \tag{12}$$

In the noiseless case, ℓ_1 minimization (11) provides the exact support of $\boldsymbol{\rho}$ when the mutual coherence μ defined in (7) is smaller than $1/(2M)$. For a general matrix $\mathcal{A}$ of size $N \times K$, with $N < K$, $\mu \geq 1/\sqrt{N}$. This implies that number of non zero components of $\boldsymbol{\rho}$ must satisfy $M < \sqrt{N}/2$. This is true regardless the resolution of the image one wants to form.

Obviously, things get more complicated when the data is noisy. In this case, the resolution is limited by the noise and, hence, it cannot be made arbitrarily small. Nevertheless, resolution can be enhanced in the presence of noise by using a so called *Noise Collector* that absorbs the unwanted signals efficiently [23]. With the *Noise Collector*, exact support is guarantee for Noise to Signal Ratios smaller than $\sqrt{N}/\sqrt{M \ln N}$, when the reflectors are well separated. When we solve for $\boldsymbol{\rho}_{d_p}$ in (5), N is the number of frequencies. Once the data are aligned, so we can use it all coherently for the final reconstruction, N is the number of frequencies multiplied by the number of spatial measurements locations.

If the reflectors are not well separated, then it can be shown that the coherent part of the solution is supported inside the vicinities of the true solution, and the incoherent part, whose support is outside them, is small [24]. The vicinities are defined as the set of pixels whose corresponding columns in $\mathcal{A}$ are almost parallel to the columns corresponding to the true support. The size of a vicinity is of the order of the Rayleigh resolution limits.

3 Numerical experiments

We consider a reflection imaging setup in optics: A single source illuminates the imaging window (IW) and a single photodetector is used to collect the reflected intensity. Then by moving the source-detector (or the sample) we obtain measurements corresponding to N locations $\boldsymbol{x}_r$ on a plane at distance $R = 1$ cm from the center of the IW.

The scanning setups used in the numerical simulations are illustrated in Figure 1: a single source-detector either moves on a circle (left) or on a two dimensional grid (right). The first scanning configuration is equivalent to the situation in which the object to be imaged is rotated at a known angles. In the results shown here we assumed that the source and the photodetector are collocated, i.e. $\boldsymbol{x}_s = \boldsymbol{x}_r$. This is not a requirement of the method. Similar reconstruction results have been obtained for other configurations, with either the distance between the source and the detector being fixed, or the source being at a fixed location and the receiver moving to collect the measurements.

Using an appropriate illumination protocol, we recover the phase cross-correlations $m^p_{ll'}$, $l, l' = 1, \dots, S$, from intensity measurements at each of the N source-detector locations for $p = 1, \dots, N$. We use $N = 16$ for both measurement configurations shown in Figure 1. We use $S = 30$ stepped frequencies $\omega_l = \omega_0 + (l-1)\Delta\omega$, $l = 1, \dots, S$, with $\frac{\omega_0}{2\pi} = 400$ THz and $\frac{\Delta\omega}{2\pi} = 5$ THz, covering the spectrum of visible light $[400, 600]$ THz.

For simplicity, the medium between the source-detector and the reflectors is homogeneous. Thus, we do not consider interfaces with refractive index mismatch in the numerical experiments. However, the proposed method extends readily for the case in which the boundaries of the sample are index mismatched. The size of the IW is 36μm $\times$ 36μm $\times$ 36μm, and the pixel size is 1.2μm $\times$ 1.2μm $\times$ 1.2μm. Thus, the number of unknowns is $31^3 = 29791$, while the total number of measurements is $30 \times 16 = 480$ and, therefore, the linear systems in Eq. (5) are underdetermined and infinitely many solutions $\boldsymbol{\rho}_{d_p}$ can fit the data. However, only $M = 10$ grid point locations in the IW have a non zero reflectivity, so an ℓ_1-minimization algorithm should be able to find their unique sparse solution.

Once these solutions $\boldsymbol{\rho}_{d_p}$ have been found, we retrieve the holographic data $b^h_p(\boldsymbol{e}_l)$, $l = 1 \dots, S$, $p = 1, \dots, N$, following the methodology proposed in Section 2 (see (9)). These data have phases that are now coherent over frequencies and scan locations and can be used for imaging the unknown reflectivity. The corresponding imaging results are shown in Figure 2. In this numerical experiment, the single source-detector rotates around the IW on a circle, as shown in the top left image of Figure 1. The top panel in Figure 2 shows the true reflectivity we seek to find. The bottom left panel is the ℓ_2-image (10), shown here for comparison purposes only. The bottom right panel in Figure 2 is the ℓ_1-image obtained by solving (11). In Figure 2, we plot the absolute value of the reflectivity normalized by its maximal value. The ℓ_1-method recovers exactly the location of the reflectors, allowing for deep tissue high-resolution imaging, while the ℓ_2-image has non-zero values at many other pixels (here we plot the thresholded KM image showing only the values above 0.3). These results illustrate that imaging with intensity-only data is as good as imaging with full data when the proposed methodology is used. Similar results are obtained when the single source-detector moves on a two dimensional grid, as shown in the top right image of Figure 1.

If, in addition to the support, one is interested in recovering the value of the reflectivity as well, then it is trivial to apply an ℓ_2-method but restricted to the found support only, which makes the problem overdetermined and simple to solve. The values of the reflectivity at the locations of the reflectors obtained this way are given in Table 1. We show the values at the scatterers location divided by the total reflectivity. We see from the results in Table 1 that the scanning configuration in which a source-detector moves on a two-dimensional grid provides a better quantitative reconstruction of the reflectivity. This has been observed consistently with other simulations not shown here. We think that this improved

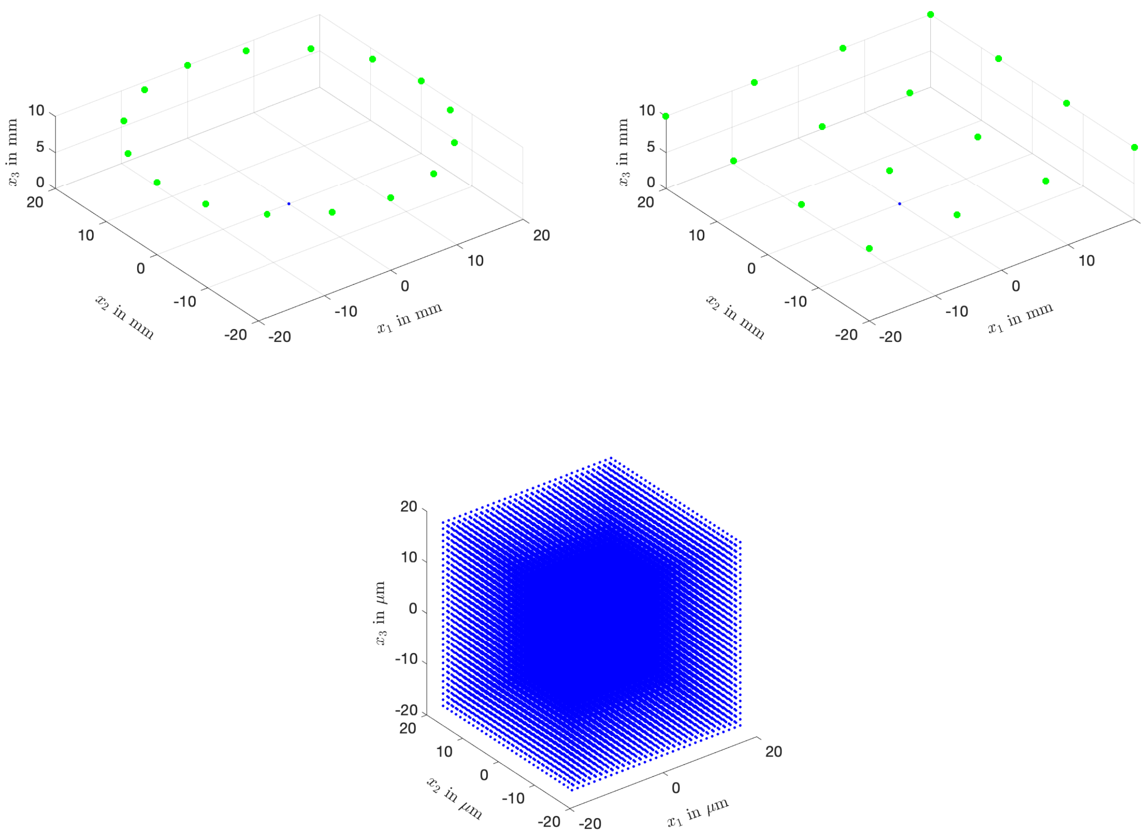

Figure 1: The scanning setups used in the numerical simulations. A single source-detector pair is conducting measurements on a plane located at a distance of 1cm from the center of the IW (green stars) and measures the reflected intensity. Two measurement configurations are considered in which the single source-detector pair either moves on a circle (left) or on a two dimensional grid (right). The measurements can be obtained by either moving the source-detector or the sample. The blue area depicts the imaging window IW. A zoom of the IW is shown on the bottom plot.

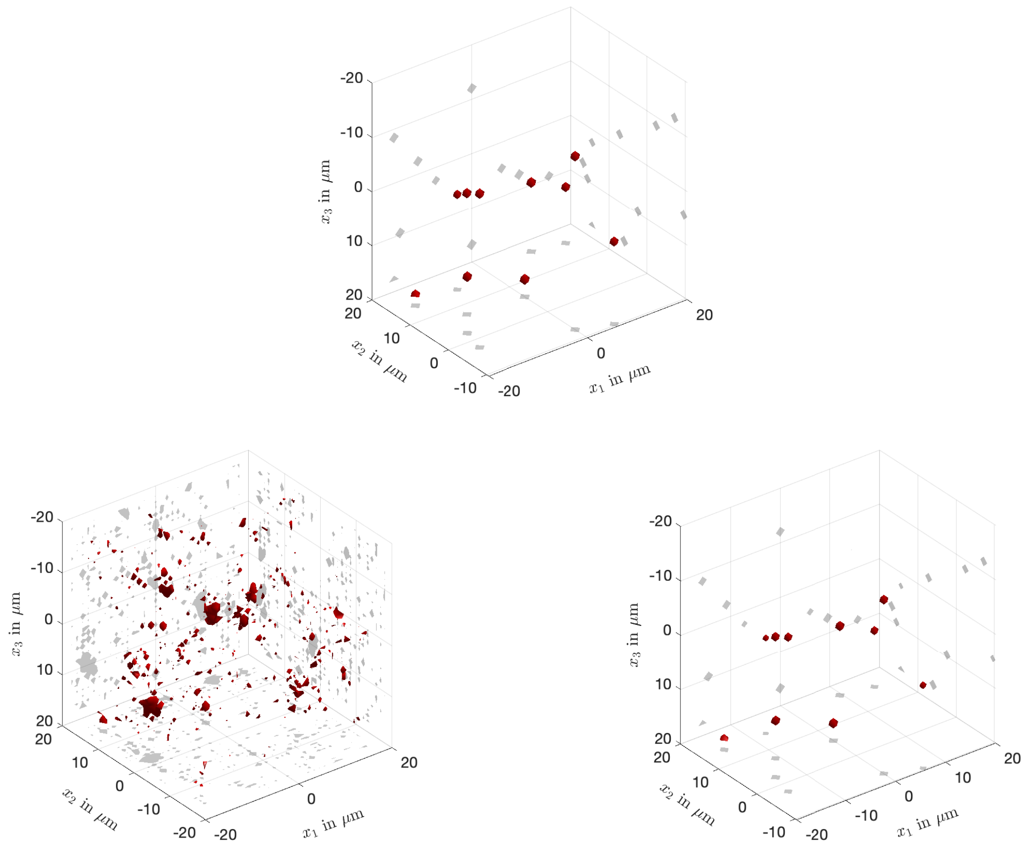

Figure 2: Top panel: the true reflectivity. Bottom left: $\boldsymbol{\rho}^{KM}$ obtained from (10). Bottom rightl: image $\boldsymbol{\rho}^{\ell_1}$ computed by solving problem (11). In all images we plot the amplitude of the complex valued reflectivity $|\boldsymbol{\rho}|$. SNR $= 10$ dB.

performance is due to the increased phase diversity of the data in this setup. Indeed, when the source-detector is moving on a circle the distance from each location to the IW is less diverse.

4 Conclusions

We presented in this paper a computational imaging methodology that allows us to obtain three dimensional images from intensity only data acquired with a single source-detector element. The method has two steps. In the first step we use frequency diverse illuminations and the polarization identities to recover full cross-correlated data. These data are known up to a phase $e^{i\theta_p}$ which is frequency independent but depends on the source-photodetector measurement location. The second step of the method aims to referring all the cross-correlated data to the same global phase $e^{i\theta_1}$. This second step recovers holographic data whose phases are coherent over different source-detector positions and frequencies. In other words, the second step synchronizes, or aligns, the data to image coherently so depth can be resolved. This is achieved by exploiting the fact that the total reflectivity must be independent of the measurement location. A key element of the method is the exact recovery of M-sparse reflectivity vectors under the usual assumption that the mutual coherence of the sensing matrix is smaller then $1/(2M)$. The proposed approach is non-iterative, in contrast with most of the algorithms used for imaging with intensities-only, and allows for exact phase recovery without any constraint on the reflectivity except the sparsity. As

Circular	2d Grid	True	$\lvert\rho_{true} - \rho_{circ}\rvert$	$\lvert\rho_{true} - \rho_{grid}\rvert$
$0.1109 - 0.0253i$	$0.1034 - 0.0270i$	$0.1014 - 0.0260i$	0.0095	0.0022
$0.0735 - 0.0009i$	$0.0860 - 0.0111i$	$0.0862 - 0.0128i$	0.0174	0.0017
$0.0970 - 0.0014i$	$0.0938 - 0.0022i$	$0.0906 - 0.0078i$	0.0091	0.0064
$0.0513 + 0.0018i$	$0.0681 + 0.0115i$	$0.0704 + 0.0097i$	0.0207	0.0029
$0.1121 + 0.0428i$	$0.1092 + 0.0382i$	$0.1061 + 0.0407i$	0.0064	0.0040
$0.1225 + 0.0403i$	$0.1081 + 0.0392i$	$0.1112 + 0.0363i$	0.012	0.0042
$0.0964 + 0.0260i$	$0.1060 + 0.0269i$	$0.1068 + 0.0313i$	0.0117	0.0045
$0.1280 - 0.0142i$	$0.1319 + 0.0019i$	$0.1327 - 0.0000i$	0.0150	0.0021
$0.0973 - 0.0304i$	$0.0905 - 0.0351i$	$0.0926 - 0.0361i$	0.0074	0.0023
$0.1109 - 0.0387i$	$0.1029 - 0.0422i$	$0.1020 - 0.0354i$	0.0095	0.0069

Table 1: True and recovered values of the reflectivity at the location of the scatterers. We give the values at the reflector locations divided by the total reflectivity. We also give the absolute value of difference between the true and the recovered reflectivity.

usually in compressive sensing this implies that the solution of highly underdetermined problems can be obtained, meaning that the number of data can be much smaller than the number of unknowns so the images can be resolved with high accuracy.

5 Funding Information

The work of MM was partially supported by spanish grant MICINN FIS2016-77892-R. The work of AN was partially supported by NSF DMS-1813943 and AFOSR FA9550-20-1-0026. The work of G. Papanicolaou was partially supported by AFOSR FA9550-18-1-0519. The work of C. Tsogka was partially supported by AFOSR FA9550-17-1-0238 and FA9550-18-1-0519.

Disclosures

The authors declare no conflicts of interest.

References

[1] D. Gabor, "Microscopy by reconstructed wave-fronts," Proc. R. Soc. Lon. Ser. A **197**, 454–487 (1949).

[2] J.Miao *et al.*, "Extending the methodology of X-ray crystallography to allow imaging of micrometer-sized non-crystalline specimens," Nature **400**, 342-344 (1999).

[3] J.R. Fienup, "Phase retrieval algorithms: a comparison," Applied Optics **21**, 2758–2768 (1982).

[4] A. M. Maiden and J. M. Rodenburg, "An improved ptychographical phase retrieval algorithm for diffractive imaging," Ultramicroscopy **109**, 1256–1262 (2009).

[5] M. Dierolf *et al.*, "Ptychographic X-ray computed tomography at the nanoscale," Nature **467**, 436–439 (2010).

[6] H. Jiang *et al.*, "Quantitative 3D imaging of whole, unstained cells by using X-ray diffraction microscopy," PNAS **107**, 11234-11239 (2010).

[7] D. Ancora *et al.*, "Phase-Retrieved Tomography enables Mesoscopic imaging of Opaque Tumor Spheroids," Scientific Reports **7**, 11854 (2017).

[8] D. Donoho, "Super-resolution via sparsity constraint", SIAM Journal on Mathematical Analysis 23, pp. 1303–1331 (1992).

[9] E. J. Candès and C. Fernandez-Granda, Towards a mathematical theory of super-resolution, Communications on Pure and Applied Mathematics 67, 906–956 (2014).

[10] L. Borcea and I. Kocyigit, "Resolution analysis of imaging with ℓ_1-optimization", SIAM J. Imaging Sci. 8, 3015–3050 (2015).

[11] J. Yuan and H. C. Berg, "Resurrection of the flagellar rotary motor near zero load", Proc. Natl. Acad. Sci. U.S.A. **105**, 1182-1185 (2008).

[12] X. Nan, P. A. Sims, and X. S. Xie, "Organelle Tracking in a Living Cell with Microsecond Time Resolution and Nanometer Spatial Precision", ChemPhysChem **9**, 707–712 (2008).

[13] Y. Sowa, B. C. Steel, and R. M. Berry, "A simple backscattering microscope for fast tracking of biological molecules", Review of Scientific Instruments 81, 113704 (2010).

[14] E. J. Candès and M. B Wakin, "An introduction to compressive sampling," IEEE signal processing magazine, 25(2), 21–30 (2008).

[15] N. Antipa *et al.*, "DiffuserCam: lensless single-exposure 3D imaging," Optica, 5(1), 1–9 (2018).

[16] A. M. Bruckstein, D. L. Donoho, and M. Elad, "From sparse solutions of systems of equations to sparse modeling of signals and images," SIAM Review **51**, 34–81 (2009).

[17] M. Moscoso *et al.*, "Synthetic Aperture Imaging With Intensity-Only Data," IEEE Transactions on Computational Imaging **6**, 87 –94 (2019).

[18] M. Moscoso *et al.*, "Coherent imaging without phases," SIAM J. Imaging Sci. **9**, 1689–1707 (2016).

[19] A. Novikov *et al.*, "Illumination strategies for intensity-only imaging," SIAM J Imaging Sci **8**, 1547–1573 (2015).

[20] M. Moscoso *et al.*, "Multifrequency interferometric imaging with intensity-only measurements," SIAM J Imaging Sci **10**, 1005–1032 (2017).

[21] M. Moscoso *et al.*, "A differential equations approach to l1-minimization with applications to array imaging," Inverse Problems **28**, 105001 (2012).

[22] N. Bleistein, J.K. Cohen, and J.W. Stockwell Jr., "Mathematics of multidimensional seismic imaging, migration, and inversion," Springer, New York, 2001.

[23] M. Moscoso *et al.*, "The Noise Collector for sparse recovery in high dimensions," Proceedings of the National Academy of Sciences, **21**, 11226–11232 (2020).

[24] M. Moscoso *et al.*, "Imaging with highly incomplete and corrupted data," Inverse Problems **36**, 035010 (2020).